

Study of methane hydrate formation and self-preservation using in-situ X-ray synchrotron tomography

V.V. Nikitin¹, G.A. Dugarov², A.A. Duchkov^{2,3}, M.I. Fokin², A.N. Drobchik², R. Mokso¹, P.D. Shevchenko⁴, F. De Carlo⁴

¹Max IV Laboratory, Lund, Sweden

²Trofimuk Institute of Petroleum Geology and Geophysics SB RAS, Novosibirsk, Russia

³Novosibirsk State University, Novosibirsk, Russia

⁴Advanced Photon Source, Argonne National Laboratory, Lemont, USA

Key Points:

- Two types of hydrate growth mechanisms were observed: into gas pockets and in water volumes.
- Only hydrates formed in water volumes were self-preserved at negative temperatures after dropping the pressure.
- Multiple fast water flows were captured during hydrate formation.

Abstract

This paper reports results of the synchrotron-based tomography experiments for studying the methane-hydrate formation/decomposition in sand samples. Fast scanning times (70 secs) provided successive images (every 2-15 min) for a detailed study of these processes. During the methane gas-hydrate formation we observed water flows that we connect to the effect of cryogenic suction due to the hydrate formation. These appeared to be multiple fast water flows in pore space followed by periods of the water position stability. Dynamic images allow identifying two types of gas-hydrate formation: into the gas pockets and inside water volumes. These two gas-hydrate types show different properties during the decomposition in the self-preservation mode - pressure drop at negative temperatures. Gas hydrate formed in water volumes remains more stable compared to hydrate formed as growing into the gas pocket. This means that the history of the gas-hydrate formation influences its behaviour at the decomposition stage (e.g gas-hydrate production).

1 Introduction

Natural gas hydrates are solid crystals that are mostly formed from water and methane. They accumulate worldwide in favorable thermobaric conditions (in permafrost regions on land and in bottom sediments offshore) and form hydrocarbon resources exceeding those in traditional and shale fields (Birchwood et al., 2010). They may also affect humanity in various other ways including flow assurance, safety issues, possible impact on ecology and climate change (Koh & Sloan, 2007). There are different ways of learning more about natural gas-hydrate systems: studying natural pressurized hydrate-bearing cores (Yoneda et al., 2017; Jin et al., 2016), geophysical characterization of natural gas-hydrate accumulations (Riedel et al., 2010), pilot experiments for the gas-hydrate production (White & McGrail, 2009; Y. Sun et al., 2014).

For better understanding of natural gas-hydrate systems we need a better knowledge of the hydrate formation/decomposition and associated processes in realistic systems. We are also interested in studying how these processes affect the rock physical properties. This is important for further development of the geophysical methods for gas-hydrate accumulations exploration and monitoring. In most cases this is done by using specialized laboratory setups for forming synthetic gas hydrates in rock samples and study their physical properties (Waite et al., 2009). It turns out that macro-properties highly depend on the sample microstructure including matrix composition, pore structure, hydrate morphology, etc.

So it is clearly beneficial to combine the laboratory experiments on forming and studying hydrate-bearing samples with their imaging at different scales. For example, different scenarios of hydrate formation result in different hydrate morphology in pore filling which considerably affects acoustic macro-properties (Waite et al., 2009; Priest et al., 2009; Dugarov et al., 2019): non-cementing (pore-filling) hydrate formation does not affect acoustic velocities much, while cementing hydrate formation type results in faster increase of acoustic properties. X-ray Computed Tomography (CT) devices are widely used to image the detailed structure of rocks which have a complicated multi-scale porous structure consisting of materials very different in properties: mineral particles, gas, multi-phase liquids. Standard X-ray CT devices require long radiation exposure time (typically from half an hour to several hours), i.e. they may provide a static image or may follow very slow processes, e.g. the hydrate formation. Micro-structure of the methane-hydrate formation was reported in (Zhao et al., 2015) with some conclusions on distribution of the gas-hydrate particles and the matrix grains. Lei and Santamarina (2018) showed that the gas-hydrate formation is displacive and segregated since hydrate extracts water from the sediments. Later Lei, Seol, et al.

(2019) showed evidence of water movement and observed 3 types of hydrate formation mechanisms: hydrate growth over sand particles, hydrate growth via water invasion into gas pockets, and extended hydrate morphology evolution via diffusion of water vapor in excess-gas environments and dissolved methane in excess-water environments. Long scanning times cause difficulties in studying time dynamics of these processes.

During the last decade, the X-ray imaging research focus has been developing towards 4D imaging of processes taking place in geomaterials. At the resolution level of 1 μm for parallel X-ray geometry (Fusseis, Xiao, et al., 2014; Saif et al., 2016), and of 20 nm for transmission X-ray microscope geometry (Andrade et al., 2016), synchrotron-based tomography is outperforming all other three-dimensional imaging methods for fast dynamic processes in bulky samples (Gibbs et al., 2015). Characteristic time for one full scan is about 0.5-3 min for microtomography and about 5-20 min for nanotomography, depending on the sample size, instrument optics and hardware limitations. Recent instrument developments (Mokso et al., 2017) allow capturing dynamic processes with temporal resolution of several seconds. Important applications of fast imaging include multi-phase fluid flow in porous rocks (Youssef et al., 2013; Blunt et al., 2013; Fusseis, Steeb, et al., 2014), deformation and geomechanical testing of samples (Baker et al., 2012; Li et al., 2015; Wang et al., 2016), and hydraulic fracturing (Kiss et al., 2015).

Studying gas-hydrates is a relatively new application that can greatly benefit from 4D X-ray imaging. Note that natural gas-hydrate systems are specifically reach in dynamic chemical-physical processing with a wide range of time scales. For example, gas-hydrate formation is a slow process that takes hours in the laboratory experiments and years to centuries in nature. Decomposition of gas hydrates is a fast process that takes several seconds. There are more dynamic processes to mention. Associated with the hydrate decomposition water/gas redistribution may take seconds to minutes. Water freezing/thawing cycles take minutes. Gas-hydrate decomposition at negative temperatures results in their self conservation when the decomposition takes minutes to hours.

In our experiments we aim at working with the methane hydrate in order to mimic natural gas-hydrate systems while increasing resolution and decreasing the scanning time to image fast processes. Compared to other research work on imaging of gas hydrates by using laboratory X-ray sources requiring several hours to measure high-resolution datasets (Chen & Espinoza, 2018; Lei, Seol, et al., 2019), we work with fast synchrotron microscopy where one dataset is measured in 70 sec. This gives us an ability to capture fast processes such as water migration inside the sample or gas hydrate decomposition. At the same time, high intense coherent beam yields improvement in reconstruction quality with employing phase retrieval procedures. In (Chaouachi et al., 2015) and (Yang et al., 2016) the gas-hydrate formation process was also studied with fast synchrotron X-ray computed tomographic microscopy. However, the gas hydrate was formed by using the Xenon gas for enhancing the contrast level between gas hydrates and water, which according to Lei et al. (2018) may demonstrate other properties than methane gas hydrates explored in reality. Xenon has much higher solubility in water than methane, and methane can diffuse faster than Xenon in water (Haynes, 2014). Thus the morphology of the resulting hydrates can be different. In this work, we instead operate with the methane gas and salt water in order to model the close to reality process.

The rest of the paper is organized as follows. In Section 2, we present the setup of the tomography experiment, a scheme for the data acquisition process, and reconstruction procedures. Section 3 presents different phenomena being observed in reconstructed images. Some of these phenomena have already been studied in other papers, but we also discovered new effects and analyze them as well. In section 4

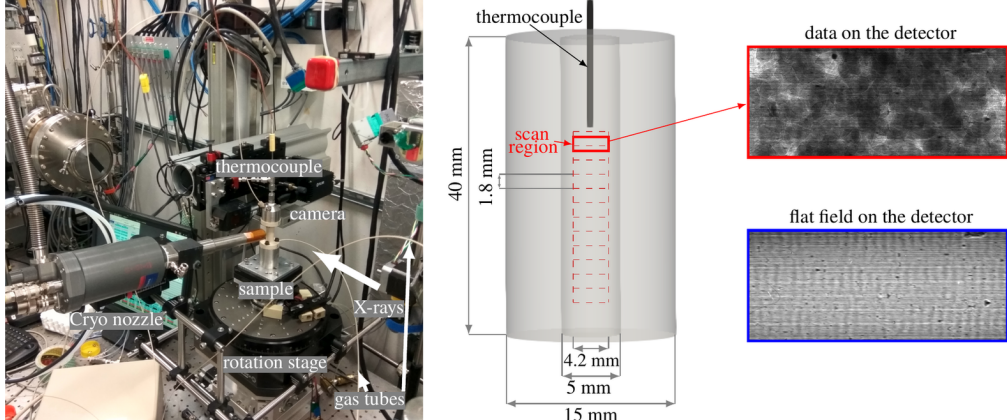


Figure 1. Setup of the tomography experiments at the 2-BM beamline of APS for studying gas-hydrate formation processes (left); and a scheme for scanning the sample (right). For analyzing the formation processes at short time periods the sample is scanned by the X-ray beam at the region marked with red color and located under the thermocouple sensor. Red dashed rectangles show scan positions for obtaining vertical data stacks through the sample. Examples of the data recorded by the detector when the sample is in and out of the field of view are marked by red and blue rectangles, respectively. The measurements were performed with 27 keV X-ray energy and 35 ms radiation exposure time.

we summarize results and present outlook for our next tomographic experiments for studying gas hydrates.

2 Experiment Setup and Data Acquisition

Tomographic experiments were conducted at the bending-magnet 2-BM beamline of the Advanced Photon Source (APS) with using the setup shown in Figure 1, left. The environmental cell is the same as the one used in (Fusseis, Steeb, et al., 2014) except that the middle vessel is produced with Polyether ether ketone (PEEK) material for better X-ray penetration. The cell is filled with wet sand, and methane gas is served via PEEK high-pressure tubes from the top and bottom sides of the cell. A thermocouple sensor for controlling the temperature in the middle of the sample is inserted from the top side. Oxford 700 Cryostream system is used for cooling the sample by a flow of nitrogen gas of low temperature. Methane gas pressure in the cell is controlled by the Teledyne ISCO D-Series single-pump system. FLIR Oryx ORX-10G-51S5M camera with 2448×2448 pixels (pixel size $3.45 \mu\text{m} \times 3.45 \mu\text{m}$) was used in a fly scan mode where projections are recorded while the sample is continuously rotated. We were able to measure data from the detector region 2448×1024 because of the reduced size of the X-ray beam passing the monochromator adjusted for the energy 27 keV. The camera recorded projections from a 100 mm-thick LuAG:Ce single-crystal scintillator, magnified through a $2 \times$ lens yielding a resulting isometric voxel size of $1.725 \mu\text{m}$.

For the experiment we used Ottawa fine white sand (grain sizes 125-250 μm), chemically pure 2.5-grade methane gas, deionized water, sodium bromide NaBr and potassium iodine KI (both SIGMA-ALDRICH, purity >99%). The sample was prepared by mixing sand with salt water and packed into the environmental cell. We performed experiments for 10% mass fraction of water in relation to sand, where water has a

certain salinity level for achieving high X-ray contrast levels between water, methane, and gas hydrate.

The right panel of Figure 1 shows a scheme for scanning the environmental cell. The sample is located inside a cylindrical vessel of the height 40 mm, with 5 mm inner and 15 mm outer diameters. The tube is made from the PEEK material, so its border is almost transparent to X-rays. The scan region used for analysis of the gas-hydrate formation process at short time periods is marked with a red rectangle. It has sizes $4.2\text{ mm} \times 1.8\text{ mm}$ and located close to the thermocouple for more accurate temperature monitoring. A few times during the experiment we also performed scanning of the whole sample to analyze water re-distribution in time. The red dashed rectangles in the figure show scan positions for obtaining vertical data stacks at long time periods. In our experiments vertical stacks are constructed by using a total of 12 scan positions.

The right-most part of Figure 1 demonstrates an example of recorded data for one projection angle after scanning the sample at the desired region, as well as a flat-field data measured where the sample is out of the field of view and used in the reconstruction process for suppressing artifacts from the detector and scintillator. For the measurements we used a monochromatic X-ray beam of the energy 27 keV and the radiation exposure time 35 ms. The parameters were chosen according to the energy range of a high photon flux level at the 2-BM beamline, and according to the optimal photon counting distribution estimated by scanning samples with similar properties.

Tomographic projections were collected in a fly scan mode while the sample was continuously rotated over 180° at 2.3°s^{-1} , yielding 70s for each 180° -scan of 2000 projection angles. We also performed tests with the number of angles satisfying the Nyquist sampling criterion for computed tomography. According to the criterion, high-quality reconstruction can be achieved by choosing the number of angles as $3/2$ of the scan width in pixels, which in our case is computed as $3/2 \cdot 2448 = 3672$. However, we did not observe any significant improvement of reconstruction quality compared to the measurements with 2000 angles.

For data processing we use Savu tomography pipeline (Wadeson & Basham, 2016) consisting of a set of plugins for tomography data processing and reconstruction. The constructed pipeline for studying gas-hydrate formation processes includes plugins for flat field correction, ring removal, and phase-retrieval filter. We also prepared our own plugin for tomography data reconstruction by using the log-polar-based method on GPU (Andersson et al., 2016).

In Figure 2 we present reconstructions with and without applying the phase-retrieval procedure by using the Paganin filter (Paganin et al., 2002). Such contrast improvement in phase-retrieved reconstruction is caused by the usage of the monochromatic coherent beam (with fixed X-ray energy 27 keV) extracted from a high-intensity white beam coming directly off the synchrotron. This effect cannot be achieved by employing standard laboratory X-ray sources.

Having a setup for scanning the sample and reconstructing the measured data we aimed at improving X-ray contrast by considering water concentrates with different salt concentration levels, as it was done, for instance, in (Lei et al., 2018). From the two most popular enhancing contrast compounds, sodium bromide NaBr and potassium iodide KI, we tested both and picked the first one since it has higher X-ray attenuation for the optimal for the 2-BM beamline energy range 20-30 keV. Then we conducted two experiments using water with different salinity. In the first experiment we used 3.5% NaBr water concentrate which is close to that of the natural sea water, for instance, in Krishna-Godavari Basin, India, where hydrate-bearing samples were explored. According to reconstruction results in Figure 2, the contrast level between gas hydrate and water is not well enough. 10% NaBr water concentrate in turn demonstrates a

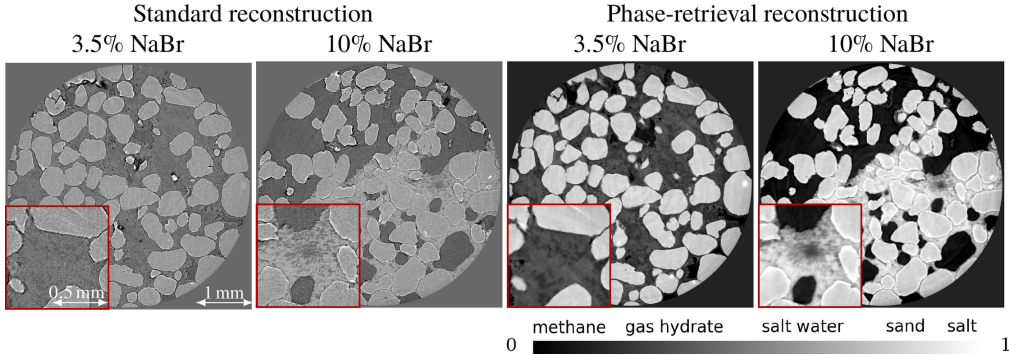


Figure 2. Reconstruction with (left) and without (right) applying the phase retrieval procedure. The presented slices have dimensions (2448 \times 2448) and were reconstructed by using the data from 2000 projection angles acquired in 70s.

higher contrast between these two materials. This salinity is also consistent with data for natural hydrate-bearing samples. Pore water salinity for the natural samples from the Mallik 2L-38 well, Mackenzie Delta, Canada, is between 4% and 12% (Winters et al., 2007). And the fluids recovered from the Mount Elbert Well, Alaska North Slope, show salinities from 2.5% to 7.5% (Torres et al., 2011). In the case of 10% salinity the attenuation coefficient of salt water is close to the coefficient for sand, which is not a problem though because sand particles are almost static during the experiment and can clearly be distinguished from water by using standard segmentation techniques. Finally, in this work we decided to use 10% NaBr water concentrate, although we do not exclude possible salt influence on the gas-hydrate formation process.

3 Imaging Results and Discussion

In this section, we summarize results by describing different phenomena observed inside the sample during the whole experiment time. To simulate gas-hydrate growth we followed certain temperature and gas pressure conditions, see (S.-C. Sun et al., 2014). Specifically, we used the temperature $T = 7^\circ\text{C}$ and the pressure $P = 10 \text{ MPa}$, which correspond to the methane-hydrate stability zone. Note that formation of ice is not possible at this positive temperature. Thus, all gnarled boundaries appearing correspond to the methane gas hydrate (water forms smooth boundaries curved according to capillary forces).

We followed the gas-hydrate formation process by scanning the sample automatically every 15 min. We also performed continuous scanning (without 15 min delays) during the hydrate decomposition process. Each full scan is used to reconstruct an image of the sample volume of size $4.2 \times 4.2 \times 1.8 \text{ mm}^3$ (2448 \times 2448 \times 1024 pixels). At certain times we performed scanning of the whole sample as a vertical stack of 12 scan regions, cf. Figure 1. For a more detailed understanding of the processes, we were zooming into the particular pore-space sub-volumes of the size $0.9 \times 0.9 \times 0.9 \text{ mm}^3$ (512 \times 512 \times 512 pixels) as shown in the following Figures 5-7. Most figures are equipped with the colorbar: black corresponds to the methane gas, dark gray - to the gas hydrate, light gray - to salt water, which is very close to even lighter gray of sand grains. White color appears later in the experiment when pure water is consumed to form the hydrate leaving very salty water or even pure salt.

Later in the text we present some observation on the dynamic processes during the hydrate formation/decomposition. In this section we find it convenient to refer to different gas-hydrate formation types as discussed in (Lei, Seol, et al., 2019):

1. Formation of the hydrate film at water-gas boundary. This hydrate-formation mechanism is natural and in the dynamic imaging the hydrate shell separating water and gas is not moving, i.e. nothing is changing much in the image.
2. Hydrate growth into the gas pocket. This mechanism of the hydrate formation requires transport of water into a pore while gas is available there. In the dynamic imaging it looks like a frost growing towards the pore center.
3. Hydrate formation in a water-filled pore. This mechanism of the hydrate formation requires transport of methane into the pore while water is available there. In the dynamic imaging it looks like a texture of darker-gray crystals of the gas hydrate appeared in the lighter water volume.

Normally, the hydrate shell (type 1) should prevent the exchange of gas and water slowing down and preventing the hydrate formation of types 2 or 3. Thus Chen and Espinoza (2018) proposed various hypotheses explaining Xenon hydrate formation in sandpack in the case when there was no obvious access to free water (thin water film that forms a capillary bridge with spontaneous water recharge or water vapor mass transport through hydrate shells). Water on hydrophobic surfaces can be transported through the gas phase with no connected water films.

3.1 Water Migration

Water migration in the pore space during hydrate formation was first observed by Gupta et al. (2006) and Kneafsey et al. (2007). This observation was confirmed later by using a micro-focus X-ray CT apparatus, cf. (Yang et al., 2015; Chen & Espinoza, 2018). It can be explained by the cryogenic suction phenomenon, i.e. capillary forces are pulling water towards regions becoming water-depleted due to hydrate formation. Water movement was also observed in (Lei, Liu, et al., 2019) and explained by cryogenic suction governed by temperature gradient generated during hydrate formation. The authors reported overall displacement of water towards the metallic walls of the chamber (that should serve as an efficient heat dissipation sink). Chen and Espinoza (2018) formed Xenon hydrate in sandpack and did not notice dramatic water movement during the hydrate formation.

We also observed water migration. We observed that water flows could happen randomly and several times during the experiment. Firstly it occurred at 1.5-2h of keeping the sample in the gas hydrate stability zone, and repeated several times in the next 12 hours. In Figure 3a, water migrated to the observable pore space. Then some amount of water transformed to hydrate, and the residual water migrated outside of the observable volume in a few stages. Water flows may break the gas hydrate structure at the beginning of the formation process, but after a certain period of time water flows just contribute to increasing of the gas hydrate volume in some random areas of pore space.

We want to make two observations on the water flow. First, water flow is not continuous. It does not move slowly for a long time as one could expect from phase transition and capillary forces. It repeatedly moves several times staying still in between. Second, it moves fast. In Figure 3 (panel 2h 15m) one can see artifacts from fast movement of a large amount of water. In panel 2h 45 min water-movement artifacts (image blurring) are observed in the zoom-in window. Similar artifacts can be seen in Figure 7 (panels 8m and 10m). It means that large water volumes move away faster than the scanning time of 70 sec.

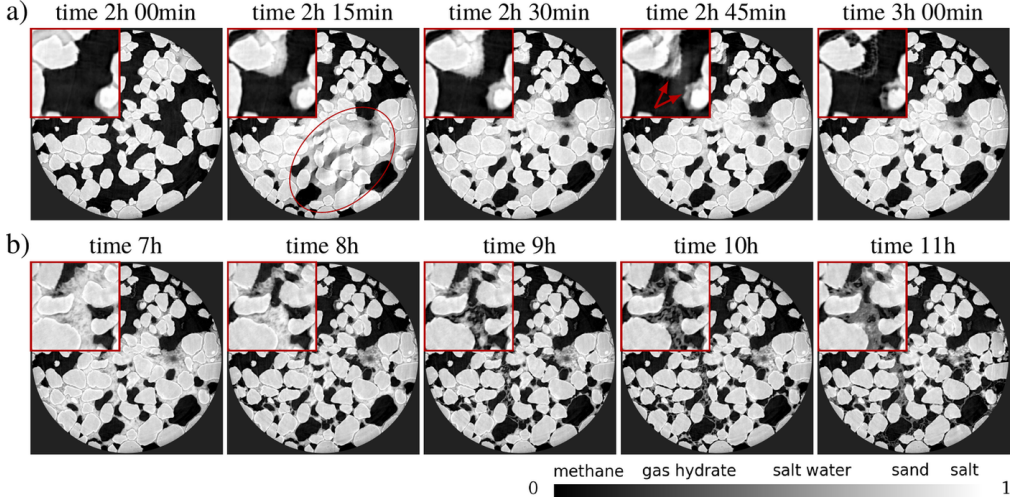


Figure 3. Water migration in the gas-hydrate formation process, caused by capillary action occurred when gas hydrates are being formed at particular locations. a) gas-hydrate formation after fast water inflow. Time frames 2h 15min and 2h 45min have motion artifacts because of fast water movement during acquisition of one data set. b) Gas hydrate structure preservation after water flows.

Note that in Figure 3 (panels 3h 00min and 9h) in zoom-in window one can see a thin hydrate structure remained after multiple water migration. It is similar to the one in the second figure in (Chaouachi et al., 2015) or can be attributed to the type 1 hydrate growth as described above. Note that if successive images are not available then these thin hydrate structures can be misinterpreted as the hydrate growth of type 2 (growth into a gas pore).

The overall pattern of water migration can be understood while comparing vertical sections through the full sample at the beginning and at the end of the experiment, as shown in Figure 4. In our experiments we did not notice a tendency of preferable hydrate formation near the sample side boundaries as reported in (Lei, Liu, et al., 2019). The reason can be due to different material of the walls of high-pressure: in our case they were plastic as opposed to metal. Overall gas hydrates have formed in the central part of the sample. After hydrate decomposition, water is redistributed in the sample more uniformly again due to capillary forces.

3.2 Different Types of Gas-hydrate Formation

In Figure 5 we show two zooms into particular pores of our sample, that illustrate the two types of the hydrate growth: growing into the gas pore (central pore in Figure 5a and right-bottom pore in Figure 5b); hydrate formation in a water-filled pore (central pore in Figure 5b). The process of growing into the pore is clearly seen in the successive images. Note that the central pore in z-slice gets fully filled with the hydrate in 8 hours while left and right pores in y-slice remain free of the hydrate. It means that continuous water supply goes into one pore and does not go into the other. The process hydrate formation in water-filled pore is shown in the central pore in Figure 5b. One can see how homogeneous gray region becomes segmented with time due to formation of hydrate particles (darker) and separation of salty water (lighter dots). In some places the salinity of the remaining water gets so high that it becomes

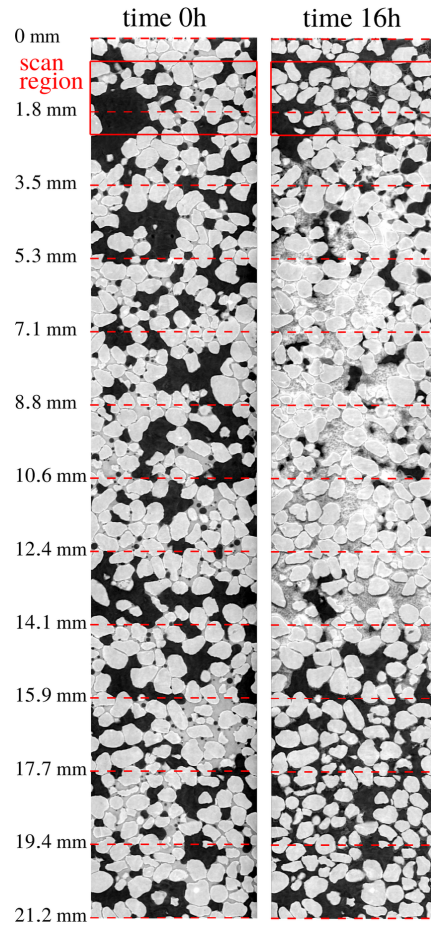


Figure 4. Water distribution at the beginning and at the end of the experiment. Each vertical stack represents 12 images merged after reconstructing the data acquired by scanning the sample in vertical direction as shown in Figure 1, right. The red rectangle corresponds to the scan region used for analysis of the gas-hydrate formation process in time.

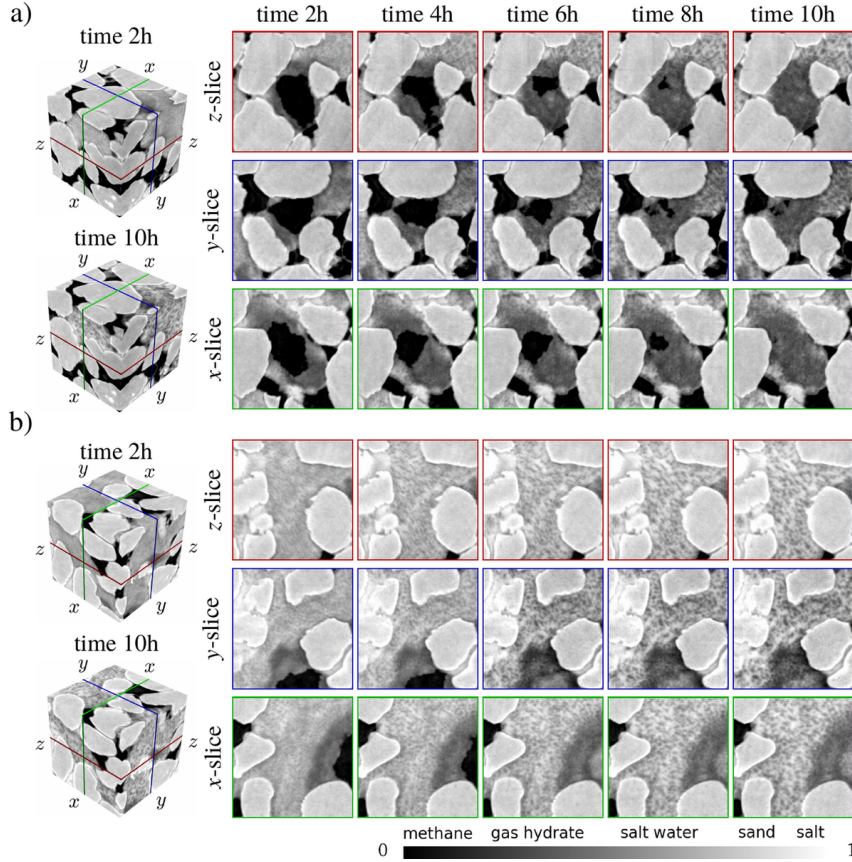


Figure 5. Gas-hydrate growth into gas pockets a), and hydrate formation in water-filled pore b) for different times (2h-10h from the experiment beginning); sand grains are static during the whole period. Left column: 3D zoomed sub-volumes; right: x -, y - and z -slices through these sub-volumes at different times.

even brighter than sand particles. Note again that x - and y -slices in Figure 5b show both types of hydrate growth.

3.3 Self-preservation Effect

In this experiment, we also check the self-preservation effect of gas hydrates, see (Stern et al., 2001; Hachikubo et al., 2011; Chuvalin et al., 2018). It is known that gas hydrates can be stored at atmospheric pressure below the melting point of ice, even though this condition is outside of the hydrate stability zone. After freezing the sample to $T = -9^\circ\text{C}$ we were gradually dropping the gas pressure from $P = 10\text{ MPa}$ (gas hydrate stability zone) to $P = 0.1\text{ MPa}$ (atmospheric pressure) and acquire tomography data for different pressure levels. As shown in Figure 6, the gas hydrate formed into gas pockets (Figure 5a) evaporates whenever the gas pressure dropped to 0.1 MPa . At the same time, the gas hydrate formed in water volumes is preserved. Note that water inflows and outflows during the pressure drops do not affect the hydrate structure. This means that the method of hydrate formation – excess-gas or excess-water (Waite et al., 2009; Manakov & Duchkov, 2017), has a great impact on the self-preservation effect of formed hydrates. And also, hydrate formation type should be taken into account in the modeling of gas production from hydrate deposits located in permafrost regions (for example, in (Y. Sun et al., 2014)).

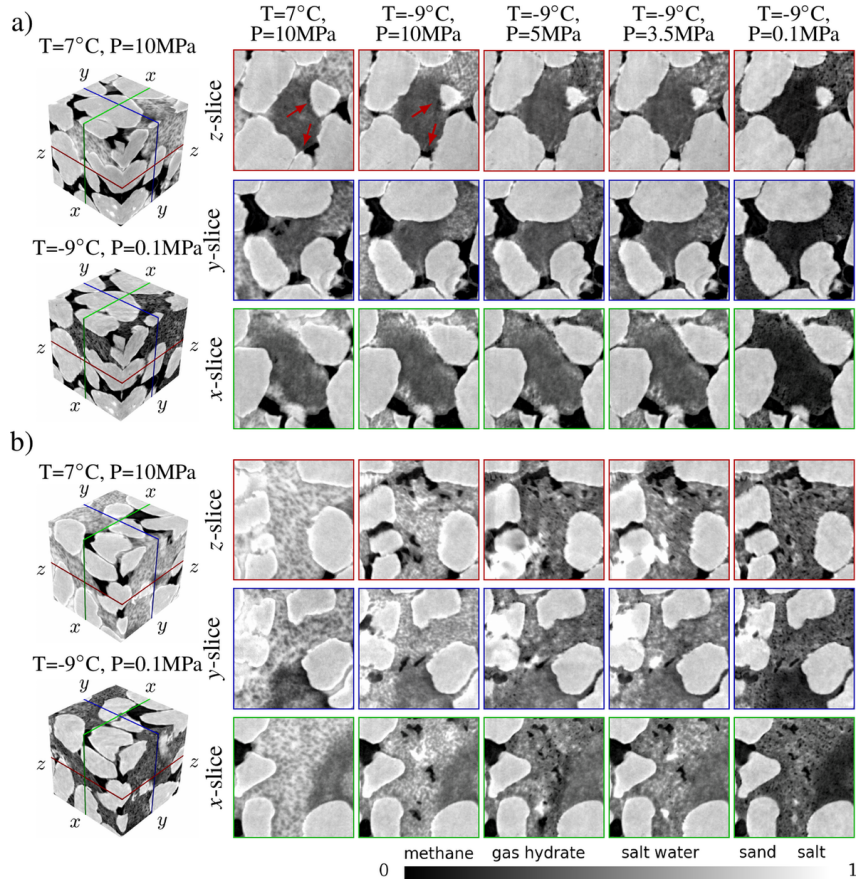


Figure 6. Self-preservation effect of gas hydrates formed into gas pockets a) and in water volumes b) after freezing the sample from the temperature $T = 7^\circ\text{C}$ to $T = -9^\circ\text{C}$ and dropping the pressure from $P = 10\text{ MPa}$ to $P = 0.1\text{ MPa}$; sand grains are moved whenever the sample is frozen. Left column: 3D zoomed sub-volumes; right: x -, y - and z -slices through these sub-volumes at different times.

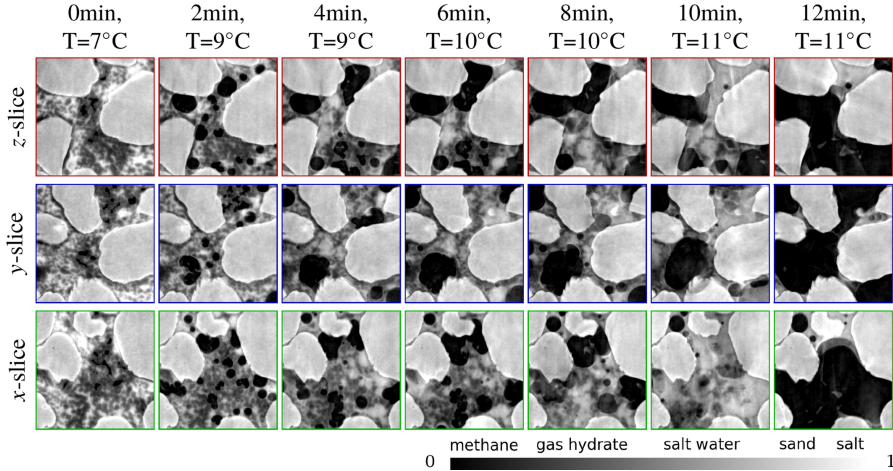


Figure 7. Capturing fast gas-hydrate decomposition process while increasing the temperature from $T = 7^{\circ}\text{C}$ to $T = 11^{\circ}\text{C}$. Slices over x , y , and z axes are extracted from the 3D zoomed sub-volume evolving with the temperature increase.

3.4 Decomposition

Synchrotron-based tomography allows capturing fast changes of the sample inner structure. Gas-hydrate decomposition process is a fast process even when it is caused by temperature increase (not pressure drop). New volumes of water and gas appear causing their redistribution in the pore space. In Figure 7 we demonstrate reconstructions of the data acquired every 2 min. We see seven successive images covering 12 minutes of the temperature growth from $T = 7^{\circ}\text{C}$ to $T = 11^{\circ}\text{C}$. We see the formation of methane bubbles at the beginning. With increasing temperature one can still follow faster movement of gas, water and hydrate particles, even though some motion artifacts in the last images.

In fig. 3 of (Yang et al., 2016) the authors show decomposition of Xenon hydrate with a 20 min interval. First, we see that the hydrates formed from Xenon and methane have different morphology. Xenon hydrates mostly form envelopes attached to the sand grains, whereas methane hydrates have more complex heterogeneous structure. Second, the Xenon hydrate started to dissociate from water-gas boundaries, forming meniscus-shaped water layers. In the methane hydrate case the decomposition process starts in the whole hydrate volume with forming of internal methane bubbles, see Figure 7. This comparison confirms the need to use methane instead of Xenon in studies of gas hydrates.

3.5 Matrix Deformation

We noticed an interesting difference between water freezing and the hydrate formation. Lei, Liu, et al. (2019) mentioned that matrix deformation (movement of sand grains) were caused the hydrate formation and freezing processes. In our experiments we see that grains do not move during the hydrate formation, for example, see Figure 5, top row. However, freezing always caused some grain movement, see Figure 6, top row. One can see that the image of the triangle-like grain changed between the first image in the row ($T = 7^{\circ}\text{C}$, $T = 10\text{ MPa}$), and the second image in the row ($T = -9^{\circ}\text{C}$, $T = 10\text{ MPa}$). While checking other images we see that freezing always caused the grain movement while the hydrate formation did not cause the particle displacement. This difference in mechanical interaction between the hydrate

particles and the matrix grains may cause a difference in mechanical properties between frozen and hydrate-bearing materials.

4 Conclusions and Outlook

In this paper, we have studied the methane gas-hydrate formation/decomposition processes by using in-situ X-ray synchrotron tomography. For our three-day tomographic experiment at the synchrotron we acquired about 500 datasets of more than 2.3Tb size in total. Fast scanning times (70 seconds) provided a lot of successive images giving a detailed insight into the processes associated with the methane-hydrate formation/decomposition.

We experimentally observed the time delay between formation of favorable PT-conditions and the actual start of the methane-hydrate formation. It took about 2 hours in the first experiment, and about 1.5 hour in the second one. We associate the beginning of the hydrate formation with the first water movement observed.

During the hydrate formation we observed water movements that we associate with the cryogenic suction (capillary forces due to water consumption into the hydrate formation). Their behaviour was interesting. It was not steady slow water flow but several fast water movements (less than 70 sec) in pore space followed by steady-state periods. These fast water flows happened in different areas at different times most likely controlled by the hydrate formation dynamics. In our experiments we did not notice a tendency of preferable hydrate formation near the sample side boundaries as reported in (Lei, Liu, et al., 2019). Possible explanation is that the walls of high-pressure chambers were made out of different materials: plastic in our case, metal in (Lei, Liu, et al., 2019). Overall observation is that in our case the gas hydrates have formed in the central part of the sample. After the hydrate decomposition, water has redistributed to form the more uniform distribution. This effect of water redistribution should be studied in more detail and should be taken into account during the laboratory studies of physical properties of hydrate-bearing samples.

During the hydrate formation we captured two types of the gas-hydrate growth: into gas pockets and inside water volumes. These two gas-hydrate types show different properties during the decomposition in the self-preservation mode - pressure drop at negative temperatures. Gas hydrate formed in water volumes remains more stable compared to hydrate formed as growing into the gas pocket. This means that the history of the gas-hydrate formation influences its behaviour at the decomposition stage (e.g gas-hydrate production).

We noticed an interesting difference between two crystallization processes: water freezing and hydrate formation. In our experiments the water freezing caused the particle pushing (displacement of the sand grains), the hydrate formation did not result in the particle displacement. This difference in mechanical interaction between the hydrate particles and the matrix grains may cause a difference in mechanical properties of frozen and hydrate-bearing geomaterials.

Our results confirm a great variety of fast processes associated with methane gas-hydrate formation-decomposition. This justifies the necessity of using fast continuous scanning of the sample with many non-delayed rotations in order to capture fast water, gas, and gas-hydrate redistribution processes. In (Nikitin et al., 2019) we introduced a method for suppressing motion artifacts in the data acquired with continuous scanning, and tested it on real data sets. Combining the developed method and fast acquisition we envision possibility of the 10-fold decrease of the scanning time that will help in suppressing motion artifacts observed in some of the images presented here.

5 Acknowledgments

This research used resources of the Advanced Photon Source, a U.S. Department of Energy (DOE) Office of Science User Facility operated for the DOE Office of Science by Argonne National Laboratory under Contract No. DE-AC02-06CH11357. The work is supported by the Swedish Research Council grant (2017-00583). The authors are grateful to A.D. Duchkov, A.Yu. Manakov, and K.E. Kuper for helpful discussions.

References

Andersson, F., Carlsson, M., & Nikitin, V. V. (2016). Fast algorithms and efficient GPU implementation for the Radon transform and the back-projection operator represented as convolution operators. *SIAM Journal on Imaging Sciences*, 9(2), 637-664.

Andrade, V. D., Deriy, A., Wojcik, M. J., Grsoy, D., Shu, D., Fezzaa, K., & De Carlo, F. (2016, Dec). Nanoscale 3D imaging at the Advanced Photon Source. *SPIE Newsroom*. doi: 10.1117/2.1201604.006461

Baker, R. D., Brun, F., O'Shaughnessy, C., Mancini, L., Fife, L. J., & Rivers, M. (2012). A four-dimensional X-ray tomographic microscopy study of bubble growth in basaltic foam. *Nature Communications*, 3, 1135.

Birchwood, R., Dai, J., Shelander, D., Boswell, R., Collett, T., Cook, A., ... others (2010). Developments in gas hydrates. *Oilfield review*, 22(1), 18–33.

Blunt, M. J., Bijeljic, B., Dong, H., Gharbi, O., Iglauder, S., Mostaghimi, P., ... Pentland, C. (2013). Pore-scale imaging and modelling. *Advances in Water Resources*, 51, 197–216.

Chaouachi, M., Falenty, A., Sell, K., Enzmann, F., Kersten, M., Haberthür, D., & Kuhs, W. F. (2015). Microstructural evolution of gas hydrates in sedimentary matrices observed with synchrotron X-ray computed tomographic microscopy. *Geochemistry, Geophysics, Geosystems*, 16(6), 1711–1722.

Chen, X., & Espinoza, D. (2018). Ostwald ripening changes the pore habit and spatial variability of clathrate hydrate. *Fuel*, 214, 614–622.

Chuvalin, E., Bukhanov, B., Davletshina, D., Grebenkin, S., & Istomin, V. (2018). Dissociation and self-preservation of gas hydrates in permafrost. *Geosciences*, 8(9). (431) doi: 10.3390/geosciences8120431

Dugarov, G. A., Duchkov, A. A., Duchkov, A. D., & Drobchik, A. N. (2019). Laboratory validation of effective acoustic velocity models for samples bearing hydrates of different type. *Journal of Natural Gas Science and Engineering*, 63, 38–46.

Fusseis, F., Steeb, H., Xiao, X., Zhu, W.-l., Butler, I. B., Elphick, S., & Mäder, U. (2014). A low-cost X-ray-transparent experimental cell for synchrotron-based X-ray microtomography studies under geological reservoir conditions. *Journal of synchrotron radiation*, 21(1), 251–253.

Fusseis, F., Xiao, X., Schrank, C., & Carlo, F. D. (2014). A brief guide to synchrotron radiation-based microtomography in (structural) geology and rock mechanics. *Journal of Structural Geology*, 65, 1 - 16. Retrieved from <http://www.sciencedirect.com/science/article/pii/S0191814114000431> doi: <http://dx.doi.org/10.1016/j.jsg.2014.02.005>

Gibbs, J. W., Mohan, K. A., Gulsoy, E. B., Shahani, A. J., Xiao, X., Bouman, C. A., ... Voorhees, P. W. (2015, Jul 03). The three-dimensional morphology of growing dendrites. *Scientific Reports*, 5, 11824. Retrieved from <http://dx.doi.org/10.1038/srep11824>

Gupta, A., Kneafsey, T. J., Moridis, G. J., Seol, Y., Kowalsky, M. B., & Sloan, E. D., Jr. (2006). Composite thermal conductivity in a large heterogeneous porous methane hydrate sample. *The Journal of Physical Chemistry B*, 110, 16384–16392.

Hachikubo, A., Takeya, S., Chuvalin, E., & Istomin, V. (2011). Preservation phenomena of methane hydrate in pore spaces. *Physical Chemistry Chemical Physics*, 13, 17449–17452.

Haynes, W. M. (2014). *CRC handbook of chemistry and physics*. CRC Press, Boca Raton, FL, USA.

Jin, Y., Konno, Y., Yoneda, J., Kida, M., & Nagao, J. (2016). In situ methane hydrate morphology investigation: natural gas hydrate-bearing sediment recovered from the Eastern Nankai Trough Area. *Energy & Fuels*, 30(7), 5547–5554.

Kiss, A. M., Jew, A. D., Joe-Wong, C., Maher, K. M., Liu, Y., Brown, G. E., & Barragar, J. (2015). Synchrotron-based transmission X-ray microscopy for improved extraction in shale during hydraulic fracturing. In *Spie optical engineering+ applications* (pp. 95920O–95920O).

Kneafsey, T. J., Tomutsa, L., Moridis, G. J., Seol, Y., Freifeld, B. M., Taylor, C. E., & Gupta, A. (2007). Methane hydrate formation and dissociation in a partially saturated core-scale sand sample. *Journal of Petroleum Science and Engineering*, 56, 108–126.

Koh, C. A., & Sloan, E. D. (2007). Natural gas hydrates: Recent advances and challenges in energy and environmental applications. *AIChE journal*, 53(7), 1636–1643.

Lei, L., Liu, Z., Seol, Y., Boswell, R., & Dai, S. (2019). An investigation of hydrate formation in unsaturated sediments using X-ray computed tomography. *Journal of Geophysical Research: Solid Earth*, 124, 3335–3349.

Lei, L., & Santamarina, J. (2018). Laboratory strategies for hydrate formation in fine-grained sediments. *Journal of Geophysical Research: Solid Earth*, 123(4), 2583–2596.

Lei, L., Seol, Y., Choi, J.-H., & Kneafsey, T. J. (2019). Pore habit of methane hydrate and its evolution in sediment matrix–laboratory visualization with phase-contrast micro-CT. *Marine and Petroleum Geology*, 104, 451–467.

Lei, L., Seol, Y., & Jarvis, K. (2018). Pore-scale visualization of methane hydrate bearing sediments with micro-CT. *Geophysical Research Letters*.

Li, T., Fan, D., Lu, L., Huang, J., Zhao, F., Qi, M., ... others (2015). Dynamic fracture of C/SiC composites under high strain-rate loading: microstructures and mechanisms. *Carbon*, 91, 468–478.

Manakov, A. Y., & Duchkov, A. D. (2017). Laboratory modeling of hydrate formation in rock specimens (a review). *Russian Geology and Geophysics*, 58(2), 240–252.

Mokso, R., Schleputz, C., & Stampanoni, M. (2017). GigaFRoST: High frame rate camera for data streaming. *J. Synchrotron radiation*, 1.

Nikitin, V., Carlsson, M., Andersson, F., & Mokso, R. (2019). Four-dimensional tomographic reconstruction by time domain decomposition. *IEEE Transactions on Computational Imaging*.

Paganin, D., Mayo, S., Gureyev, T. E., Miller, P. R., & Wilkins, S. W. (2002). Simultaneous phase and amplitude extraction from a single defocused image of a homogeneous object. *Journal of microscopy*, 206(1), 33–40.

Priest, J. A., Rees, E. V., & Clayton, C. R. (2009). Influence of gas hydrate morphology on the seismic velocities of sands. *Journal of Geophysical Research: Solid Earth*, 114(B11).

Riedel, M., Willoughby, E. C., & Chopra, S. (2010). *Geophysical characterization of gas hydrates*. Society of Exploration Geophysicists.

Saif, T., Lin, Q., Singh, K., Bijeljic, B., & Blunt, M. J. (2016). Dynamic imaging of oil shale pyrolysis using synchrotron X-ray microtomography. *Geophysical Research Letters*, 43(13), 6799–6807. Retrieved from <http://dx.doi.org/10.1002/2016GL069279> (2016GL069279) doi: 10.1002/2016GL069279

Stern, L., Circone, S., Kirby, S., & Durham, W. (2001). Anomalous preservation

of pure methane hydrate at 1 atm. *Journal of Physical Chemistry B*, 105(9), 1756–1762.

Sun, S.-C., Liu, C.-L., Ye, Y.-G., & Liu, Y.-F. (2014). Phase behavior of methane hydrate in silica sand. *The Journal of Chemical Thermodynamics*, 69, 118–124.

Sun, Y., Li, B., Guo, W., Lü, X., Zhang, Y., Li, K., ... Qu, L. (2014). Comparative analysis of the production trial and numerical simulations of gas production from multilayer hydrate deposits in the Qilian Mountain permafrost. *Journal of Natural Gas Science and Engineering*, 21, 456–466.

Torres, M., Collett, T., Rose, K., Sample, J., Agena, W., & Rosenbaum, E. (2011). Pore fluid geochemistry from the Mount Elbert gas hydrate stratigraphic test well, Alaska North slope. *Marine and Petroleum Geology*, 28, 332–342.

Wadeson, N., & Basham, M. (2016). Savu: a Python-based, MPI framework for simultaneous processing of multiple, N-dimensional, large tomography datasets. *arXiv preprint arXiv:1610.08015*.

Waite, W. F., Santamarina, J. C., Cortes, D. D., Dugan, B., Espinoza, D., Germaine, J., ... others (2009). Physical properties of hydrate-bearing sediments. *Reviews of geophysics*, 47(4).

Wang, M., Lu, L., Li, C., Xiao, X., Zhou, X., Zhu, J., & Luo, S. (2016). Deformation and spallation of a magnesium alloy under high strain rate loading. *Materials Science and Engineering: A*, 661, 126–131.

White, M., & McGrail, P. (2009). Designing a pilot-scale experiment for the production of natural gas hydrates and sequestration of CO₂ in class 1 hydrate accumulations. *Energy Procedia*, 1(1), 3099–3106.

Winters, W., Waite, W., Mason, D., Gilbert, L., & Pecher, I. (2007). Methane gas hydrate effect on sediment acoustic and strength properties. *Journal of Petroleum Science and Engineering*, 56, 127–135.

Yang, L., Falenty, A., Chaouachi, M., Haberthür, D., & Kuhs, W. F. (2016). Synchrotron X-ray computed microtomography study on gas hydrate decomposition in a sedimentary matrix. *Geochemistry, Geophysics, Geosystems*, 17(9), 3717–3732.

Yang, L., Zhao, J., Liu, W., Li, Y., Yang, M., & Song, Y. (2015). Microstructure observations of natural gas hydrate occurrence in porous media using microfocus X-ray computed tomography. *Energy & Fuels*, 29, 4835–4841.

Yoneda, J., Masui, A., Konno, Y., Jin, Y., Kida, M., Katagiri, J., ... Tenma, N. (2017). Pressure-core-based reservoir characterization for geomechanics: Insights from gas hydrate drilling during 2012–2013 at the eastern Nankai Trough. *Marine and Petroleum Geology*, 86, 1–16.

Youssef, S., Deschamps, H., Dautriat, J., Rosenberg, E., Oughanem, R., Maire, E., & Mokso R. (2013). 4D imaging of fluid flow dynamics in natural porous media by ultrafast X-ray microtomography. *SCA Proceedings*, 12.

Zhao, J., Yang, L., Liu, Y., & Song, Y. (2015). Microstructural characteristics of natural gas hydrates hosted in various sand sediments. *Physical Chemistry Chemical Physics*, 17(35), 22632–22641.